Elucidating the Vibrational Fingerprint of the Flexible Metal-Organic Framework MIL-53(Al) Using a Combined Experimental/Computational Approach

Alexander E. J. Hoffman,[†,‡] Louis Vanduyfhuys,[†] Irena Nevjestić,[‡] Jelle Wieme,[†] Sven M. J. Rogge,[†] Hannes Depauw,[¶] Pascal Van Der Voort,[¶] Henk Vrielinck,[*,‡] and Veronique Van Speybroeck[*,†]

†*Center for Molecular Modeling, Ghent University, Technologiepark 903, 9052 Zwijnaarde, Belgium*

‡*Department of Solid State Sciences, Ghent University, Krijgslaan 281-S1, 9000 Ghent, Belgium*

¶*Center for Ordered Materials, Organometallics and Catalysis, Ghent University, Krijgslaan 281-S3, 9000 Ghent, Belgium*

E-mail: Henk.Vrielinck@UGent.be; Veronique.VanSpeybroeck@UGent.be

Supporting Information

Contents

S1 Experimental details **S3**

S1.1 Characterization by powder X-ray diffraction S3

S1.2 Influence of dilution on the spectra S3

S1.3 Comparison of experimental techniques S4

S2 Computational details **S10**

S2.1 Lattice parameters S10

S2.2 Comparison of DFPT and Berry phase approach S10

S2.3 Measure for correspondence and determination of scaling factor S12

S3 Additional spectra **S15**

S3.1 IR spectrum from dynamic DFT calculations S15

S3.2 IR spectrum in range 2800–4000 cm^{-1} S18

S3.3 Raman spectrum in range 2800–4000 cm^{-1} S19

S4 Mode identification **S20**

S5 Visualization of the IR active modes in far-IR **S22**

S5.1 IR active modes in CP and LP phases S22

S5.2 IR active mode only present in the LP phase S24

S6 Low-frequency vibrations **S25**

S6.1 Closed pore phase S25

S6.2 Large pore phase S27

S7 Videos of the vibrational modes **S29**

References **S30**

S1 Experimental details

S1.1 Characterization by powder X-ray diffraction

The transitions between the different phases of MIL-53(Al) occur easily. Consequently, to measure vibrational spectra of the pure phases experimentally, it is important to know under which external conditions a certain phase is present. This can be examined by powder X-ray diffraction (PXRD). In Figure S1, the evolution of the PXRD patterns with air pressure and temperature are visualized together with the PXRD patterns of the NP-h, CP and LP phases. From the PXRD patterns, we can clearly see that under ambient conditions, MIL-53(Al) is completely in the NP-h phase. When lowering the pressure by pumping, the NP-h phase transforms to the CP phase within a short period of time. This process could be followed both in PXRD (Figure S1a) and in situ Fourier transform infrared (FTIR) spectroscopy. Therefore, both the CP and NP-h phases are readily obtained. The LP phase, in contrast, could only be measured experimentally by increasing the temperature as evidenced by PXRD measurements (Figure S1b). Moreover, as the transformation to the NP-h phase occurs very easily in a humid atmosphere, the LP phase has to be created in situ during spectroscopic characterization. In this study, this could only be achieved using a diffuse reflectance FTIR setup, limited to the mid-IR range.

S1.2 Influence of dilution on the spectra

In the main article we state that the influence of the matrix material is negligible when recording transmittance IR spectra of MIL-53(Al) in the NP-h phase. This is clearly visible in Figure S2, where the transmittance IR spectra of the NP-h phase with KBr and polyethylene (PE) pellets as matrix material are compared in the range 400-700 cm^{-1}. We observe that all absorption bands are located at exactly the same position. Some of these bands have a slightly different intensity, which is very likely more related with differences (in thickness, density, homogeneity) between reference and sample pellets than with the interaction of the

matrix material with MIL-53(Al).

Furthermore, we observed that also in the CP phase the dilution of the material in KBr does not affect the spectral features as is clear from Figure S5. In contrast, the measurement of the transmittance IR spectrum of the CP phase upon dilution in PE and pellet pressing is affected by the matrix material (see Figures S3 and S4). The nature of the influence of PE on MIL-53(Al) is at present unclear and requires further investigation. For this reason ATR experiments in vacuum, which allow to record both the mid-IR and far-IR range of the spectrum without exposing the sample to air have been performed for the CP phase. In the mid-IR range, this spectrum agrees very well with transmittance and diffuse reflectance spectra (see Figure S5).

S1.3 Comparison of experimental techniques

In the paper we report experimental IR spectra obtained by transmittance IR, ATR IR, and DRIFT. Comparison between these spectra is only possible if the influence of the experimental technique on the spectrum is small. In Figure S5, we compare the mid-IR spectrum of the CP phase of MIL-53(Al) recorded by the three experimental techniques. While the spectra do not match exactly, exhibiting small intensity differences and frequency shifts, the IR active bands can clearly be distinguished in each of the three spectra. The spectrum that differs the most from the other two is the DRIFT spectrum due to the Kubelka-Munk transformation, necessary to generate an absorption spectrum out of a diffuse reflectance spectrum. However, we also notice minor dissimilarities between the transmittance IR and ATR IR spectra. This can clearly be illustrated by looking at the symmetric and antisymmetric stretching modes of the carboxylic group. In Figure S5, the intensities of the strongly IR active symmetric stretch mode are the same for all techniques, as they are rescaled in that way, but the intensities of the antisymmetric stretch mode differ. Furthermore, the modes are found at slightly different frequencies. We see that the vibrational bands in the ATR IR spectrum are red shifted compared to the transmittance IR spectrum. These shifts

differ between modes, but are small, ranging from 0.5 to 6 cm^{-1}. The red shift of the ATR IR spectrum can largely be explained by the pressure produced by the lever, which is necessary to provide good contact. To investigate the importance of this pressure on the spectrum, we recorded an ATR IR spectrum without lowering the lever. This yields a spectrum of lower quality, but still allowed us to examine the effect of the lever. In Figure S6, ATR IR spectra obtained with and without lowering the lever are compared with each other. We notice that the spectrum recorded without pressure is blue shifted compared to the situation with pressure. In addition, also the intensities evolve towards the ones observed in the transmittance IR spectrum. It is clear that, although the pressure is small, it is sufficient to compress the MIL-53(Al) powder, which results in a small decrease of the pore volume. This gives rise to small frequency shifts and intensity changes.

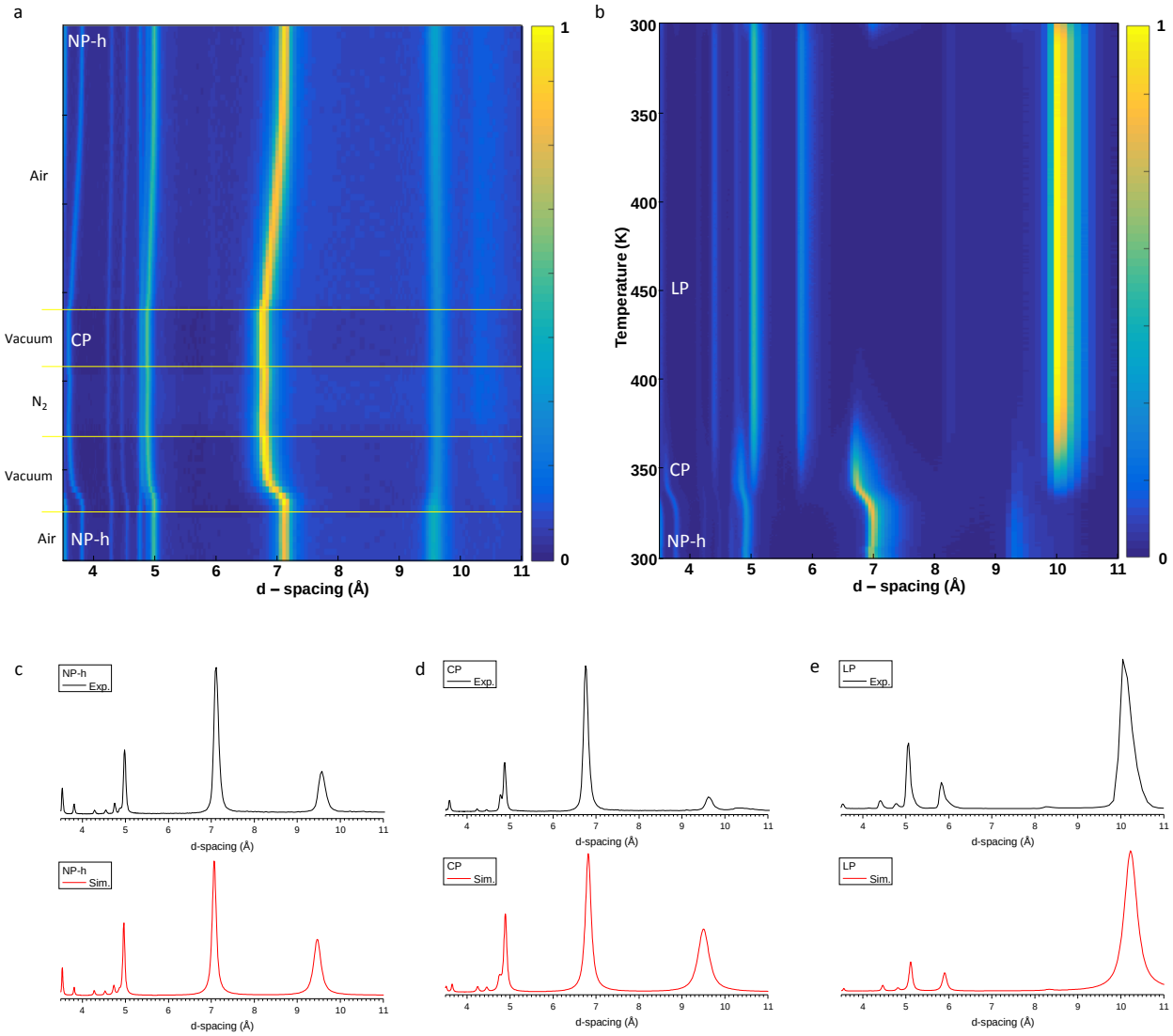

Figure S1: Powder X-ray diffraction (PXRD) patterns of activated MIL-53(Al) in air, λ=1.54056 Å. 2θ is converted to d-spacing in Å via Bragg's law. (a) PXRD measurements at room temperature with different air pressures. Intensities are represented in color scale with the maximum normalized to 1. The sample was initially in the NP-h phase. The bottom yellow line indicates the moment when the pump was switched on and the sample started dehydrating. The second yellow line indicates when N_2 gas was applied to the sample. After that, N_2 was evacuated and the sample was left in air until it returned to the NP-h phase. (b) PXRD measurements showing the temperature dependence of MIL-53(Al). Intensities are represented in color scale with the maximum normalized to 1. The sample was in the NP-h phase at the start of the experiment. While heating, transition to the CP phase occurs around 350 K. Further heating induces a pure LP phase. By cooling the sample in air, the transition from the LP to the NP-h phase is observed near room temperature. (c),(d),(e) Experimental and simulated PXRD patterns of MIL-53(Al) in the NP-h, CP and LP phase, respectively. The experimental patterns for the NP-h and CP phases were taken from part (a) of this figure (300 K), while the experimental pattern for the LP phase was taken from part (b) (at 450 K). The parameters used for the simulations are taken from Nevjestić *et al.*[1]

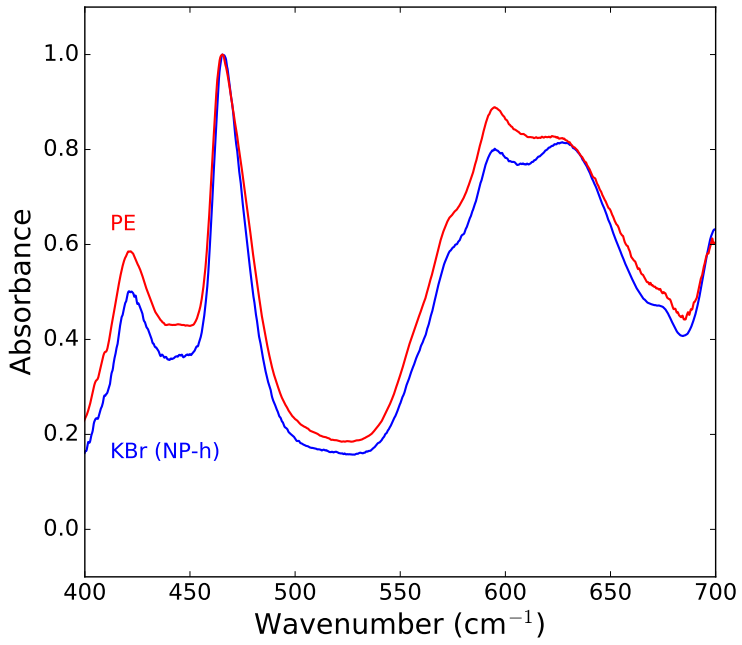

Figure S2: Transmittance IR spectra of MIL-53(Al) in the NP-h phase in the range 400-700 cm^{-1}. One of the spectra uses KBr as matrix material (blue), while the other one uses PE (red).

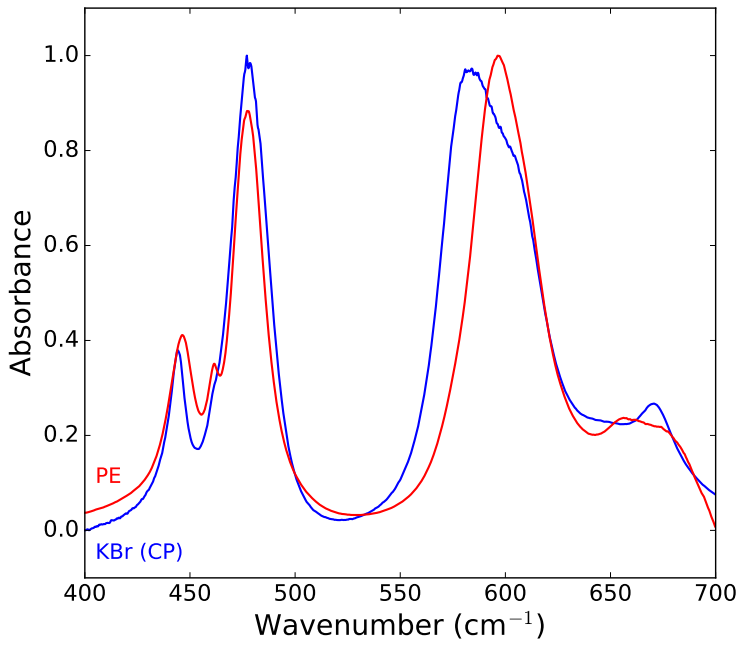

Figure S3: Transmittance IR spectra of MIL-53(Al) in the range 400-700 cm^{-1}. The blue curve represents the IR spectrum of the CP phase with KBr as matrix material. The red curve shows the IR spectrum of MIL-53(Al) with PE as matrix material prepared under the same conditions. The spectra differ significantly, however.

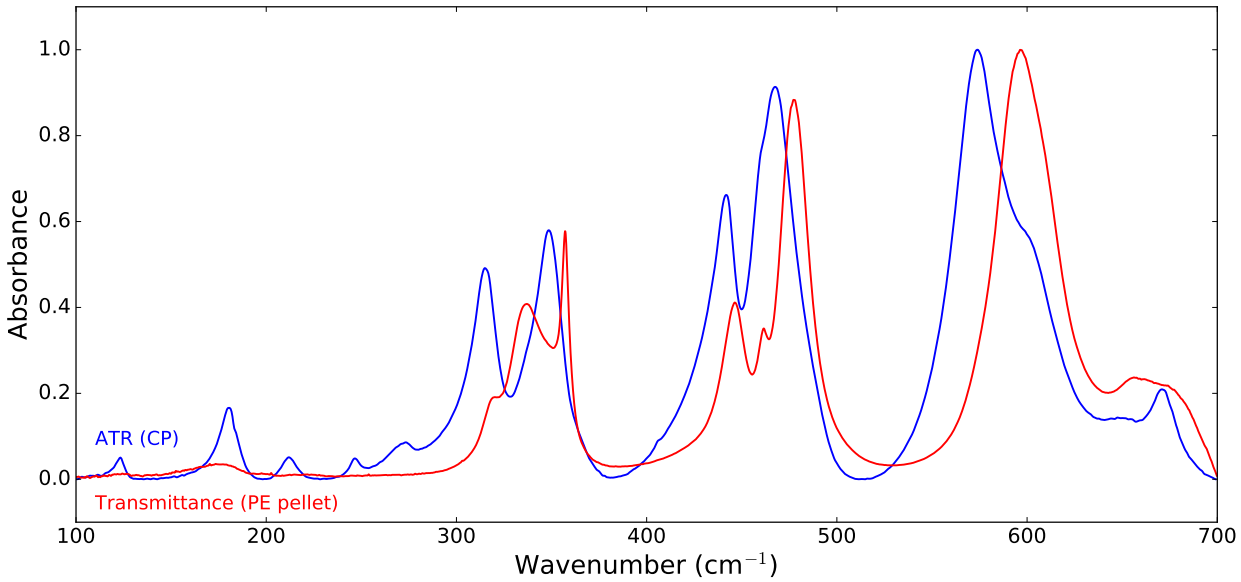

Figure S4: Comparison of the ATR IR spectrum of MIL-53(Al) in the CP phase with the transmittance IR spectra of MIL-53(Al) in a PE pellet in the range 100-700 cm^{-1}.

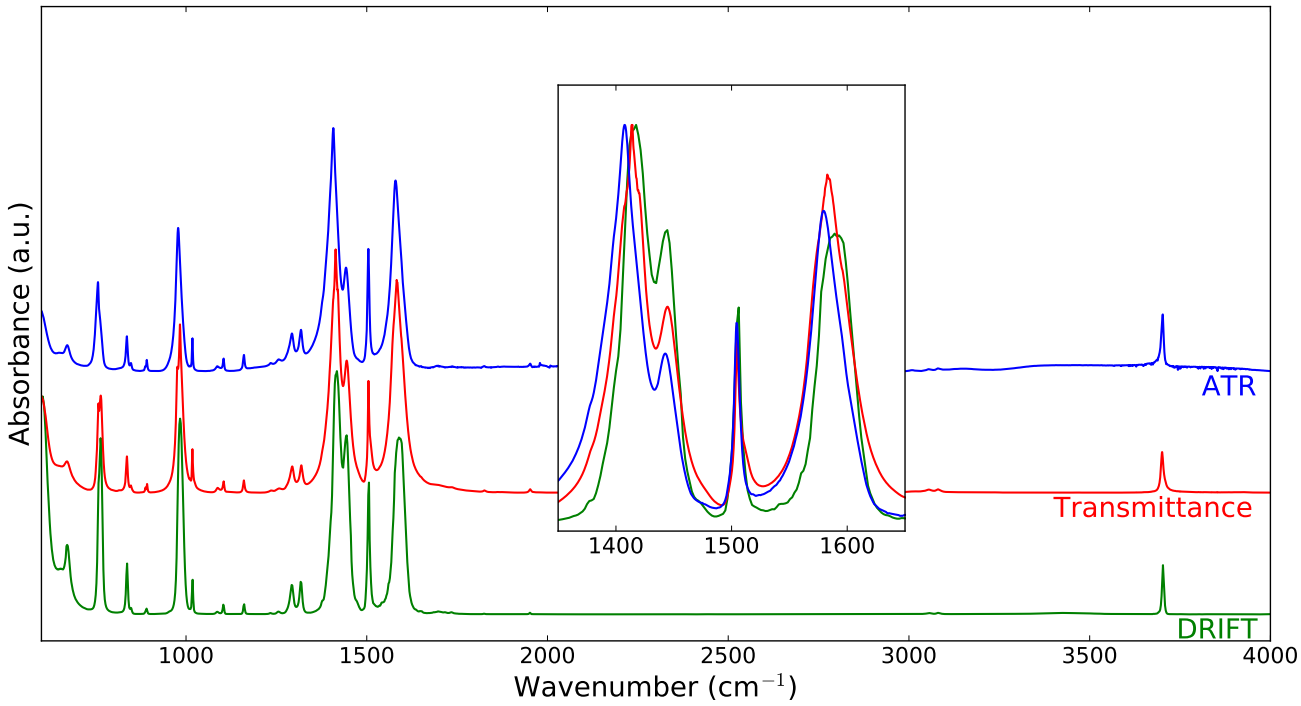

Figure S5: Comparison of the experimental mid-IR spectra (600–4000 cm^{-1}) of the CP phase of MIL-53(Al) obtained by ATR IR spectroscopy (blue), transmittance IR spectroscopy (red), and DRIFT spectroscopy (green).

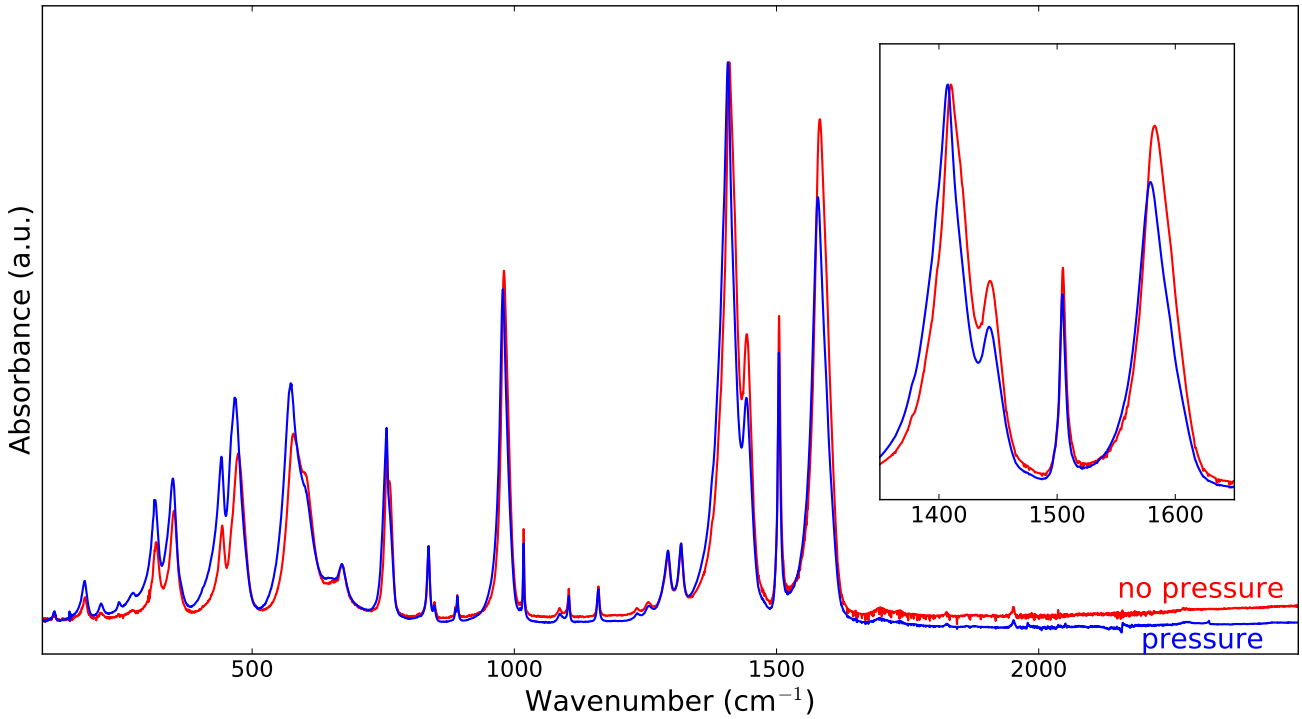

Figure S6: ATR IR spectra of the CP phase of MIL-53(Al) in the range 100–2500 cm^{-1} once with pressure delivered by the lever (blue) and once without pressure (red).

S2 Computational details

S2.1 Lattice parameters

Table S1: Comparison of the computational lattice parameters (0 K) of MIL-53(Al) with the experimental values (300 K) obtained in the work of Liu *et al.*[2] The lattice parameters of the phases of our own samples were not measured. All values were reported using a unit cell convention different from the one reported by Liu *et al.*[2] The definition for the angle θ and the distance D can be found in the work of Vanduyfhuys *et al.*[3]

	a (Å)	b (Å)	c (Å)	α (°)	β (°)	γ (°)	θ (°)	D (Å)	V (Å^3)
DFT CP	19.248	6.654	6.608	90.0	90.0	95.4	37.9	20.4	843
DFT LP	17.059	6.663	12.574	90.0	90.0	89.2	72.8	21.2	1429
Exp. CP[2]	19.096	6.609	7.055	90.0	90.0	95.1	40.6	20.4	887
Exp. LP[2]	16.744	6.636	12.847	90.0	90.0	90.0	75.0	21.1	1428

S2.2 Comparison of DFPT and Berry phase approach

In the article, we reported the theoretical IR spectrum obtained via density functional perturbation theory (DFPT). However, the calculation via DFPT had to be performed without dispersion corrections. In Figure S7, we verify that this approach gives qualitatively the same results as the Berry phase approach, where dispersion corrections were taken into account. Apparently, dispersion corrections are of minor importance in the actual calculation of the IR spectrum. Nevertheless, they are essential in the optimization procedure.

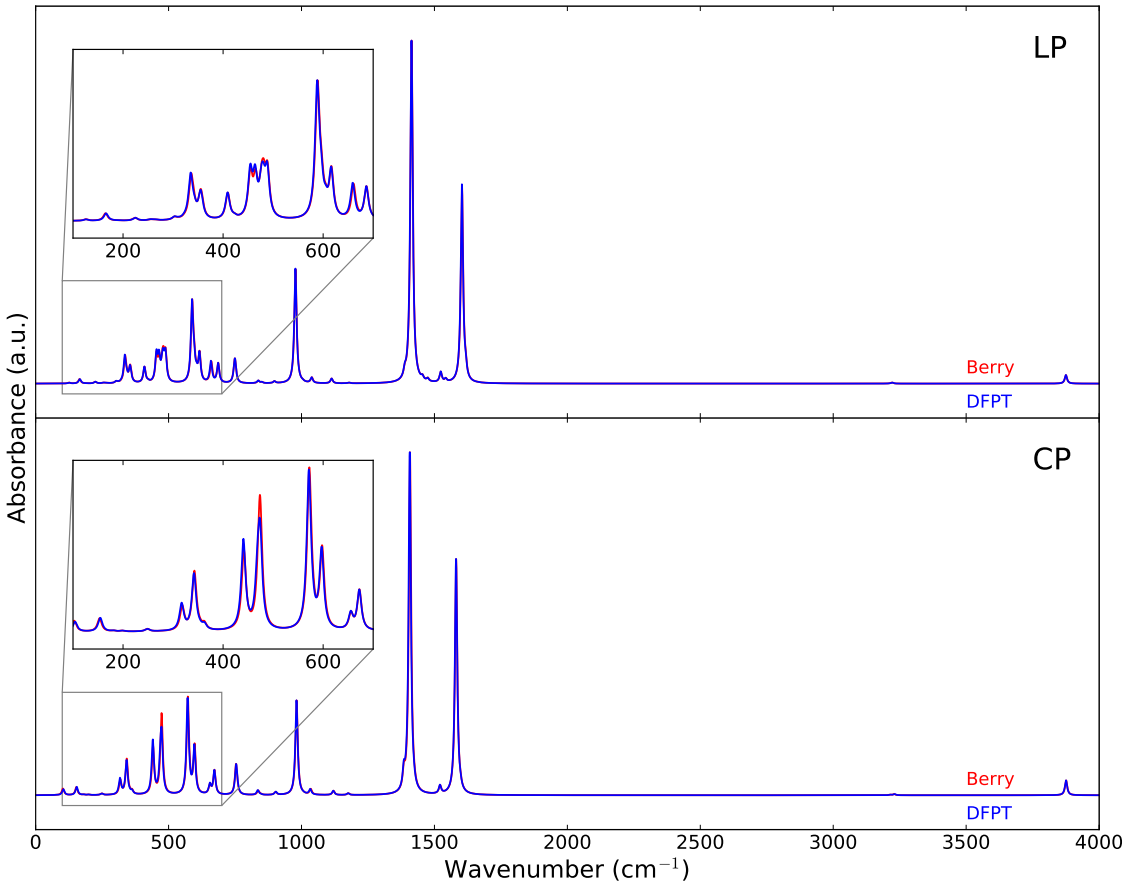

Figure S7: Comparison of the theoretical IR spectra obtained by calculation via DFPT (blue) and the Berry phase approach (red) in the range 0–4000 cm^{-1}. Top: LP phase. Bottom: CP phase. The theoretical IR spectra were blue shifted with a scaling factor of 1.025 and received a Lorentzian line shape with FWHM of 10 cm^{-1}.

S2.3 Measure for correspondence and determination of scaling factor

In order to quantitatively determine the correspondence of our simulated spectra with the experimental result, we calculated the similarity index (SI), which evaluates the correlation between two functions:[4,5]

$$\mathrm{SI} = \frac{\int f(\sigma)g(\sigma)\,\mathrm{d}\sigma}{\sqrt{\int f^2(\sigma)\,\mathrm{d}\sigma \int g^2(\sigma)\,\mathrm{d}\sigma}} \tag{1}$$

Here $f(\sigma)$ and $g(\sigma)$ represent the intensities of the simulated and experimental spectrum at frequency σ. An SI value of zero means absolutely no correspondence between both spectra, while an SI value of one indicates that the spectra are identical. As the peaks in an IR and Raman spectra are narrow, comparison of the simulated and experimental spectrum using the SI value only makes sense when they are evaluated on the same frequency scale. Accordingly, we also need to determine the correct scaling factor for the simulated frequencies. Another important factor in evaluating the SI value is the broadening applied to the simulated spectra. In this work we applied a Lorentzian line shape with a full width at half maximum (FWHM) of 10 cm^{-1} to the IR spectra obtained by static DFT calculations in order to resolve all the spectral features. The Raman spectra resulting from AIMD did not receive additional broadening as their intrinsic broadening was sufficient. In Table S2, the optimal scaling factor and their SI values are represented for several situations.

All SI values in Table S2 are larger than 0.5, from which we conclude that our simulated spectra are in quantitative agreement with the experimental spectra. For the case of the static DFT IR spectrum of the CP phase with a FWHM of 28 cm^{-1} compared to the ATR IR spectrum recorded with lowered lever, we even observe an SI value of 0.95, which indicates an excellent agreement between the spectra. When we only look at the far-IR spectrum, the SI value becomes 0.96 with the same scaling factor. So the correspondence holds for both the mid- and far-IR. We note that for higher broadening factors, we can get a higher SI value,

Table S2: Optimal scaling factor and corresponding SI value for the simulated IR and Raman spectra of the CP and LP phases. We compare different experimental techniques and different broadening factors.

Simulated spectrum	**Measurement (range in cm^{-1})**	**lever**	**FWHM**[1] **(cm^{-1})**	**CP**		**LP**	
				scaling	**SI**	**scaling**	**SI**
IR (static)	ATR FTIR (100–4000)	✓	10	1.025	0.82		
			28	1.025	0.95		
		✗	10	1.028	0.79		
			28	1.028	0.91		
	DRIFT (600–4000)	✗	10	1.032	0.74	1.028	0.70
			28	1.033	0.86	1.029	0.84
IR (AIMD)	ATR FTIR (100–4000)	✓	0	1.036	0.63		
			20	1.035	0.82		
		✗	0	1.039	0.58		
			20	1.039	0.77		
	DRIFT (600–4000)	✗	0	1.044	0.55	1.040	0.68
			20	1.043	0.75	1.041	0.83
Raman (AIMD)	FT-Raman (150–4000)	✗	0	1.035	0.55	1.022	0.53
			10	1.034	0.60	1.024	0.56

[1]Additional broadening factor.

but this makes several vibrational modes less resolved. For that reason, broadening factors smaller than the optimal ones were used for the spectra reported in the paper. Furthermore, we observe different optimal scaling factors when we compare simulations with DRIFT and ATR IR measurements, which is caused by the Kubelka-Munk transition (see Section S1). We also observe different optimal scaling factors between ATR IR measurements with and without lowered lever, because of changes in density of the experimental sample (see Section S1). Besides the scaling factor, also the SI value differs for both ATR IR measurements. The situation with lowered lever shows a slightly higher agreement with our simulated spectrum, probably because the volume of the denser experimental structure matches better with the

volume of our simulated structure. While small differences in optimal scaling factors between the spectra of the CP and LP phases exist, the same scaling factor was used for both phases in order to compare their spectra. As the combination of ATR IR measurements with lowered lever with simulations of the CP phase yield the highest SI values, we applied a scaling factor of 1.025 and 1.035 to all static and dynamic DFT spectra, respectively.

S3 Additional spectra

S3.1 IR spectrum from dynamic DFT calculations

AIMD simulations were performed to determine the theoretical Raman spectra of the CP and LP phases of MIL-53(Al). Therefore, the dipole moment of the zero-field situation was calculated every 2.5 fs allowing us to calculate the IR spectrum without additional computational cost. In Figure S8, the IR spectra obtained from dynamic DFT simulations are compared with the static DFT results to get an idea of the anharmonicities and temperature effects. As the resolution of the AIMD spectra is modest due to limited simulation time, a supplementary Lorentzian line shape is applied to smoothen the spectra. This also improves the correspondence with experiment (see Section S2.3). First of all, we notice a general increase in intensity for the dynamic spectrum of the CP phase compared to the static spectrum, which is not observed for the LP phase. This is in agreement with the experimental results and shows that our dynamic simulations are able to take into account the lower experimental symmetry of the system, because it samples over more configurations. Furthermore, a weak IR active mode is noted around 1300 cm^{-1} in the AIMD simulation of the CP phase that corresponds to the $\nu 3$ ring mode. This follows the experimental result and was not observed in the static simulation. However, the spectral shifts between the CP and LP phase appearing in the experimental spectra and predicted by static simulations are most often not captured by the AIMD simulations (see Table S3). The shifts in the symmetric and asymmetric stretching modes of the metal-oxide backbone do emerge in the dynamic simulation. For wavenumbers below 700 cm^{-1}, the dynamic simulation for the CP phase performs worse than its static counterpart, which could be due to the limited simulation time.

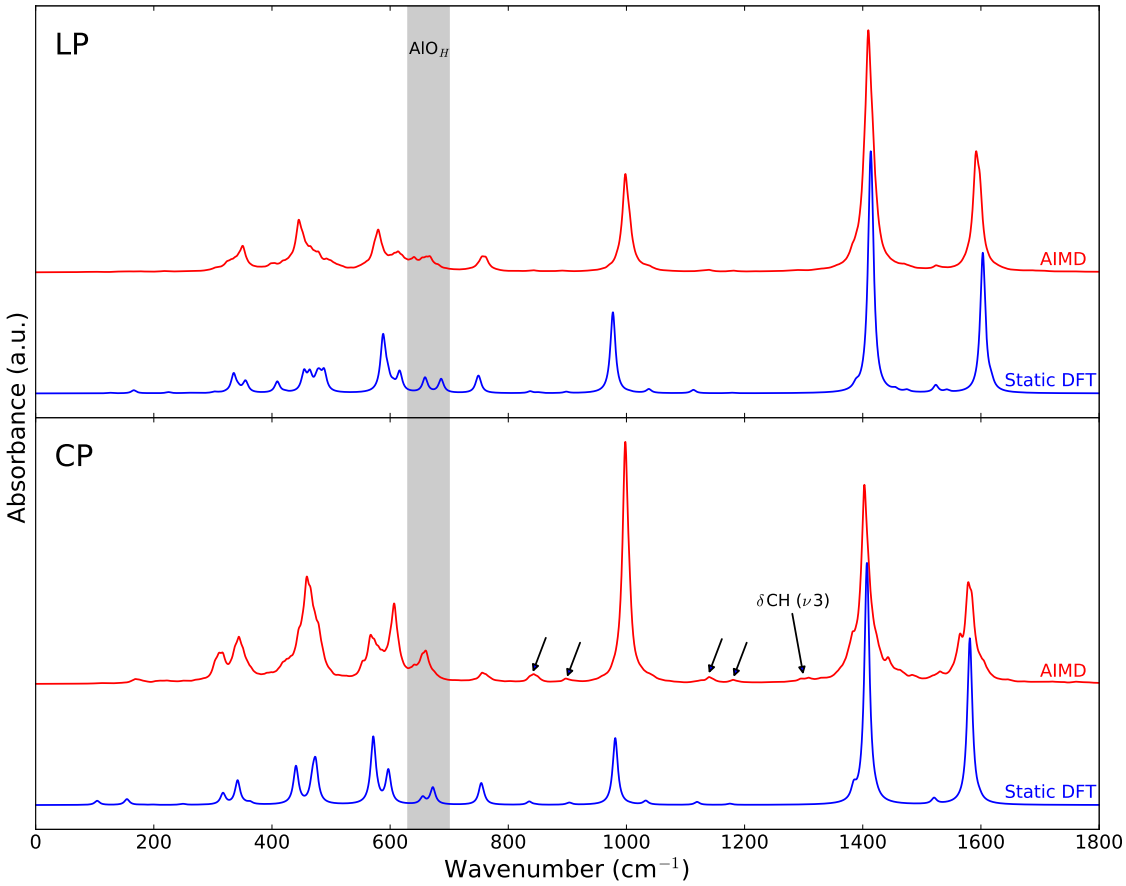

Figure S8: Comparison of the IR spectra of the LP (top) and CP (bottom) phase of MIL-53(Al) obtained by static DFT (blue) and AIMD (red) simulations in the range 0–1800 cm^{-1}. All theoretical IR spectra were blue shifted with a scaling factor of 1.025 (static DFT) or 1.035 (dynamic DFT) and received a(n) (additional) Lorentzian line shape with a FWHM of 10 cm^{-1}.

Table S3: Experimental and theoretical frequencies (dynamic) of the vibrational modes characteristic for the CP-to-LP transition along with the spectral shifts between both phases.

Vibrational mode	**Experiment (cm^{-1})**			**Simulation[1] (cm^{-1})**		
	CP	**LP**	$\Delta_{\mathbf{LP-CP}}$	**CP**	**LP**	$\Delta_{\mathbf{LP-CP}}$
νAlOAl$_{sym}$	653	657	4	641	640	-1
νAlOAl$_{as}$	671	680	9	660	667	7
ωCH	764	756	-8	756	756	0
δCCC + δCO$_2$	847	851	4	863	863	0
δOH	983	991	8	998	998	0
δCCC + δCH	1018	1026	8	1038	1038	0
νCC + δCH	1160	1163	3	1180	1180	0
ν_{sym}CO$_2$	1415	1418	3	1403	1409	6
νCC + δCH	1505	1509	4	1530	1523	-7
ν_{as}CO$_2$	1589	1597	8	1579	1592	13

[1]The values are multiplied with a scaling factor of 1.035.

S3.2 IR spectrum in range 2800–4000 cm^{-1}

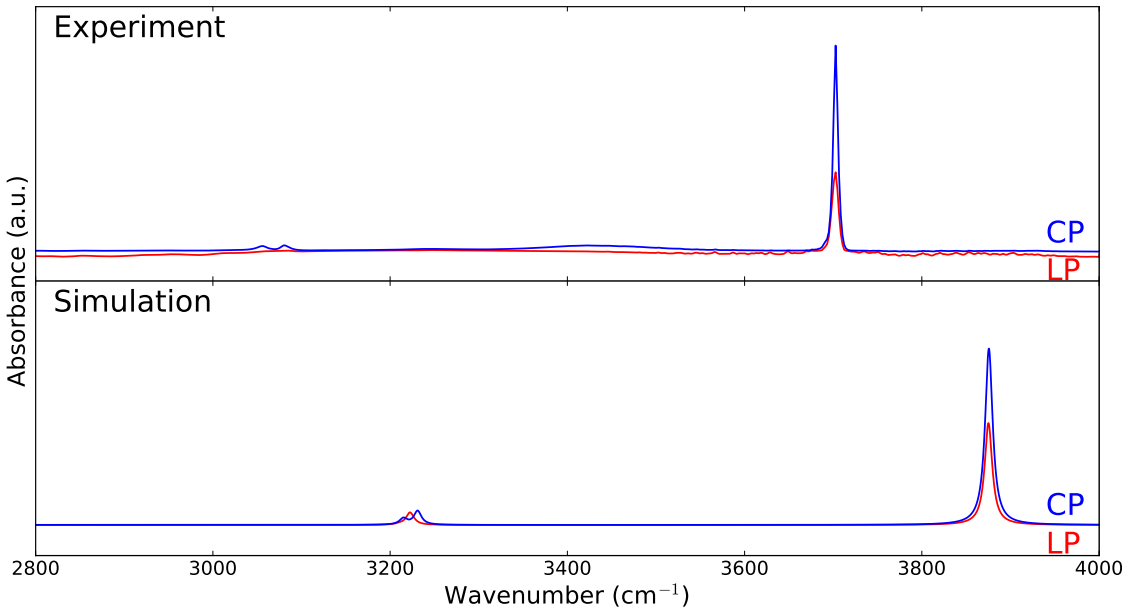

Figure S9: Comparison of DRIFT spectra (top) and theoretical IR spectra obtained by static DFT calculations (bottom) for the CP (blue) and LP (red) phase in the range 2800–4000 cm^{-1}. The theoretical spectrum was blue shifted with a scaling factor of 1.025 and received a Lorentzian line shape with a FWHM of 10 cm^{-1}. In contrast to the other vibrational modes, the blue shift degrades the correspondence between the experimental and theoretical spectrum.

S3.3 Raman spectrum in range 2800–4000 cm^{-1}

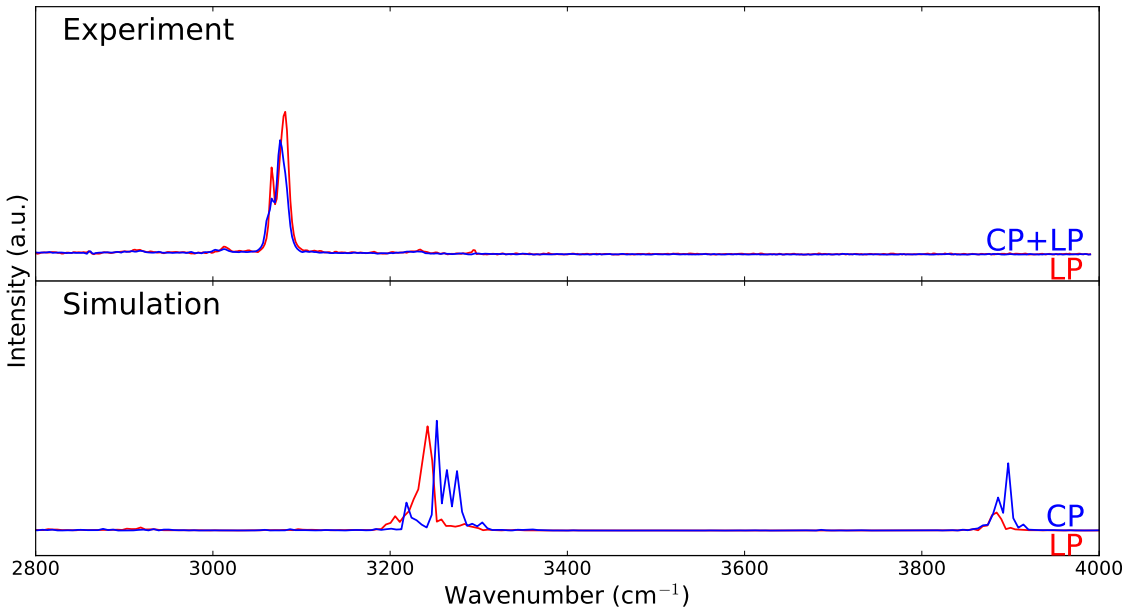

Figure S10: Comparison of experimental (top) and theoretical (bottom) Raman spectra for the CP (blue) and LP (red) phase in the range 2800–4000 cm^{-1}. The theoretical spectrum was obtained by AIMD simulations and is blue shifted with a scaling factor of 1.035. As was the case for static simulations, the blue shift degrades the correspondence between the experimental and theoretical spectrum.

S4 Mode identification

Table S4: Identification of the optically active (IR or Raman) vibrational bands of MIL-53(Al) in the CP and LP phase. Both the experimental and computational bands are given. Below 600 cm^{-1} the experimental IR spectrum of the LP phase is not recorded. Raman active modes below 300 cm^{-1} in the experimental spectrum could not be identified.

Vibrational mode	**Activity**	**Experiment (cm^{-1})**		**Simulation[1] (cm^{-1})**	
		CP	**LP**	**CP**	**LP**
νOH	IR	3702	3702	3876	3875
νCH (ν7a,b + ν20a,b)	Raman	3061/3076	3066/3081	3214/3231	3211/3222
νCC (ν8a)	Raman	1616	1618	1644	1644
$\nu_{as}CO_2$	IR	1579	1596	1581	1564
νCC + δCH (ν19a)	IR	1503	1508	1521	1523
$\nu_{sym}CO_2$	Raman	1441/1475	1460/1477	1441/1473	1455/1475
$\nu_{sym}CO_2$	IR	1406	1417	1407	1413
ν_{as}CCC (ν14)	IR	1377	1377	1385	1388
ν_{as}CCC (ν14) (From Ref.[6])	IR	1317	1318		
δCH (ν3)	IR	1292	1291	1310	1304
νCC + δCH (ν9a)	Raman	1182	1183	1206	1204
νCC + δCH (ν18a)	IR	1160	1163	1175	1178
νCC + δCH (ν9a)	Raman	1143	1149	1163	1166
δCH (ν15)	IR	1103	1103	1120	1113
δCCC + δCH (ν18a)	IR	1018	1026	1033	1038
δOH	IR	983	991	981	977
ωCH (ν17b)	IR	891	888	904	899
δCCC + δCO_2 (ν6a)	Raman	871	873	879	882
δCCC + δCO_2	IR	837/847	837/851	836/846	837/851
ωCC (ν4)	Raman	823	823	828	822
ωCH (ν11)	IR	764	756	755	750
νAlOAl$_{as}$	IR	671	680	672	686
νAlOAl$_{sym}$	IR	653	657	655	659
νAlO_C + νAlO_H	Raman	630	630	633	634
νAlO_C	IR	600		597	616
νAlO_C + δCO_2	IR	573		571	588

[1]The values are multiplied with a scaling factor of 1.025.

Vibrational mode	Activity	Experiment (cm^{-1})		Simulation[1] (cm^{-1})	
		CP	LP	CP	LP
δAlOAl + δCCC	Raman	479		483	
δAlOAl + δCCC + δOH	IR + Raman		479		488
ωCC + ωCH (ν16b)	IR	467		474	480
ωAl +δAlOAl + ωCH	IR	459		469	464
ωAl + δOH + ωCH	IR	441		441	454
δAlOAl + δOH	IR				409
AlOAl backbone deformation	IR	314/348		317/342	335/355
δOH + scissoring of octahedron	IR				262/267
δOH + scissoring of octahedron	IR	273		250	253
δOH + scissoring of octahedron	IR				225
δOH + linker shearing	IR	246		198	222
linker shearing + scissoring of octahedron	IR	212		176	
δOH + scissoring of octahedron	IR	180		155	166
δOH + rocking of metal-oxide backbone	IR	122		104	126

[1]The values are multiplied with a scaling factor of 1.025.

S5 Visualization of the IR active modes in far-IR

S5.1 IR active modes in CP and LP phases

Four different IR active modes in the far-IR spectrum of the CP and LP phases are visualized here. (a) Stretching mode of the aluminum atom with the oxygen atoms of the carboxylic group (597 cm^{-1} in CP phase, 616 cm^{-1} in LP phase). (b) Combined in-plane and out-of-plane vibration of the ring structure coupled with rocking of the aluminum atom (ν16b ring mode) (441 cm^{-1} in CP phase, 454 cm^{-1} in LP phase). (c) Metal-oxide backbone deformation (342 cm^{-1} in CP phase, 355 cm^{-1} in LP phase). (d) Vibration of the hydroxyl group coupled with scissoring of the oxygen atoms of the carboxylic group (155 cm^{-1} in CP phase, 166 cm^{-1} in LP phase).

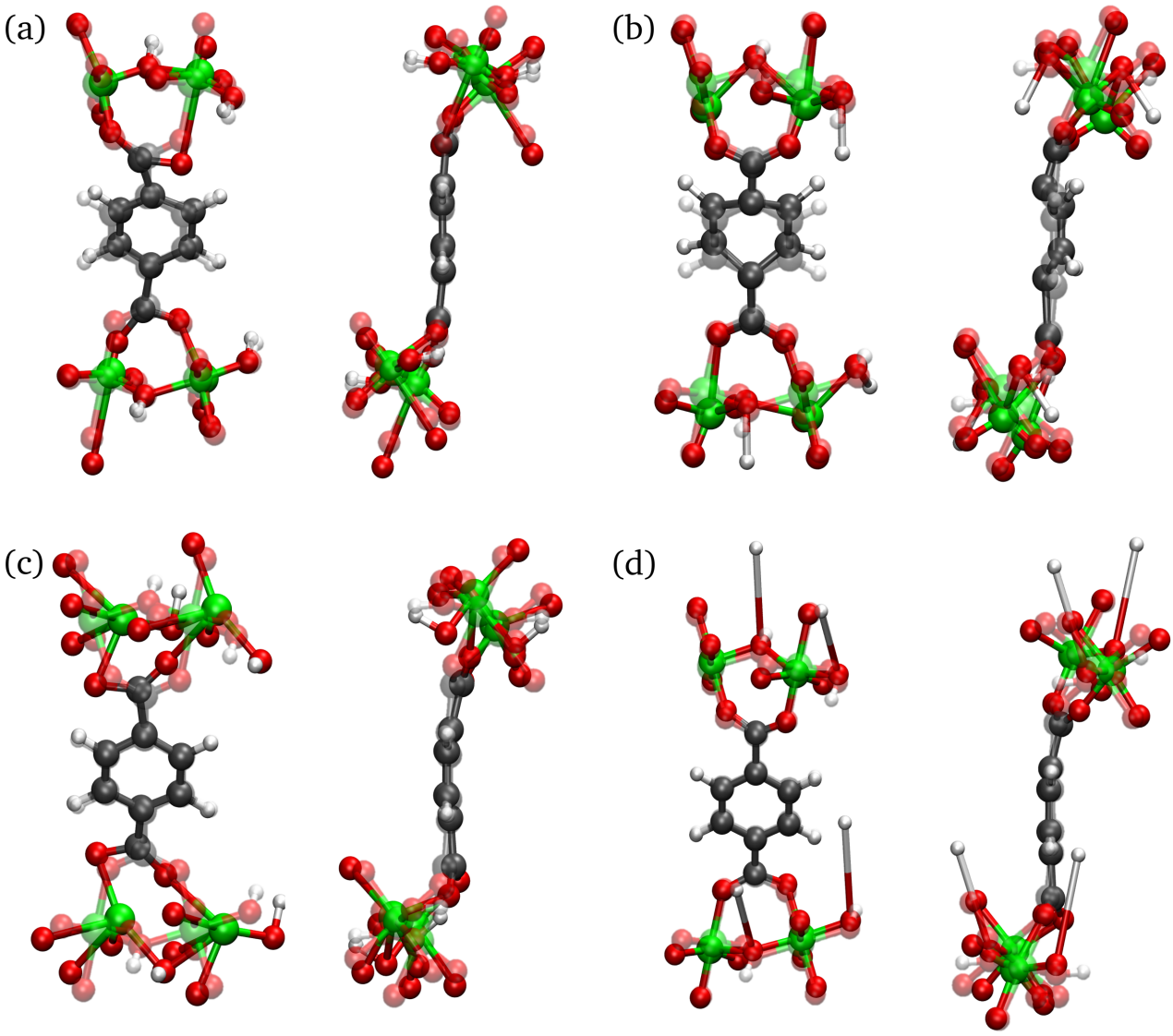

Figure S11: Visualization of four IR active modes in the far-IR region. (a) Stretching of AlO_C. (b) Combined in-plane and out-of-plane vibration of aromatic ring with rocking of aluminum atom (ν16b). (c) Metal-oxide backbone deformation. (d) Vibration of hydroxyl group with scissoring of metal octahedra. Videos of these modes are available in Section S7.

S5.2 IR active mode only present in the LP phase

In the paper we discuss two aluminum oxide bending modes, which are IR active in the LP phase, but not in the CP phase. One of these aluminum oxide bending modes is located at 483 cm^{-1} in the CP phase and at 488 cm^{-1} in the LP phase following from static DFT simulations. The bending mode in the LP phase is coupled with an additional bend of the hydroxyl group, which makes it IR active. This is not the case for the CP phase and the mode remains IR inactive. Additionally, this particular bending mode is coupled with shrinking of the aromatic ring resulting in Raman activity. Accordingly, this mode appears in our experimental and theoretical Raman spectrum.

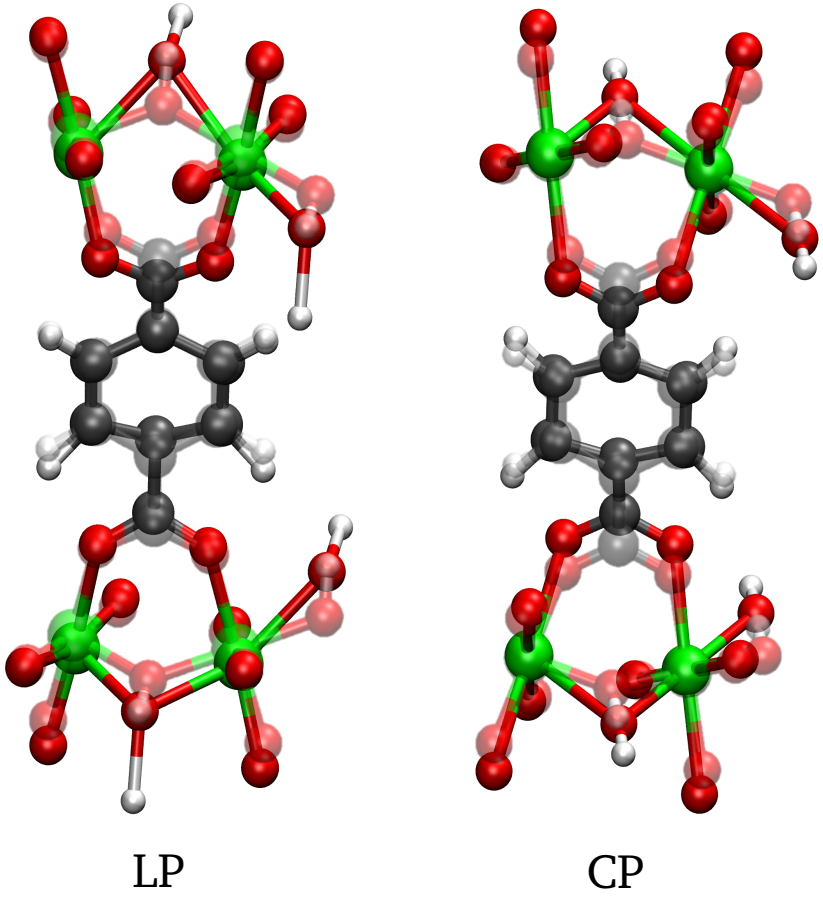

Figure S12: AlOAl bend mode in the LP phase with additional bend of the hydroxyl group (left) and in the CP phase without additional bend of the hydroxyl group (right). Videos of this mode are available in Section S7.

S6 Low-frequency vibrations

S6.1 Closed pore phase

Table S5: Vibrational modes of the CP phase of MIL-53(Al) in the region 0–310 cm^{-1} obtained from static DFT simulations. The wavenumbers are multiplied with a scaling factor of 1.025.

Wavenumber (cm^{-1})	**Mode description**
11.1	Rotation of metal-oxide backbone + trampoline motion
27.0	Rocking of metal-oxide backbone (perpendicular)
42.6	Rocking of metal-oxide backbone (longitudinal)
68.9/69.0	Linker rotation
71.6	Rocking of metal-oxide backbone + trampoline motion
88.6	Rotation of metal-oxide backbone + trampoline motion
104.1	Rocking of metal-oxide backbone + δOH
107.5	Linker shearing
109.9	δOH + deformation of octahedron
117.7	Rotation of metal-oxide backbone
122.7	Trampoline motion + linker shearing
131.6	Rotation of metal-oxide backbone + linker shearing
137.7	Trampoline motion
138.5	Trampoline motion + rotation of octahedron
141.0	Rocking of linker + deformation of octahedron
142.7	Trampoline motion + rotation of octahedron + linker shearing
151.2/151.7	Linker rotation
154.5/158.7	Scissoring of octahedron + δOH
170.5/172.2	Scissoring of octahedron + linker rocking
179.7	Linker rocking
180.4	Linker shearing + scissoring of octahedron

Wavenumber (cm^{-1})	**Mode description**
191.4	Metal-oxide backbone rocking + δOH
194.9	δOH + linker rocking
198.3	δOH + linker shearing
200.2	Linker rocking + deformation of octahedron
208.9	Scissoring of octahedron + trampoline motion
222.2	Scissoring of octahedron + δOH + linker shearing
227.0	Scissoring of octahedron + seesaw motion of linker
235.6	Rocking of metal-oxide backbone + seesaw motion of linker
240.9	δOH + seesaw motion of linker
245.1	Deformation of octahedron
246.2	Undulating motion of linker + δAlOAl + δOH
249.7	Scissoring of octahedron + δOH
262.5	Scissoring of octahedron + rocking of aluminum atom + linker rocking
277.1	Scissoring of octahedron + δAlOAl
277.1	Scissoring of octahedron + rocking of octahedron
277.5	Deformation of octahedron + linker shearing + δOH
278.8	Scissoring of octahedron + linker rocking + δOH
280.1	Deformation of octahedron + linker shearing
283.7	Rocking of aluminum atom + linker rocking
289.4	Deformation of octahedron + δAlOAl
300.3	Scissoring of octahedron + metal-oxide backbone deformation + linker rocking + δOH
303.3	Bending of metal-oxide backbone + scissoring of octahedron

S6.2 Large pore phase

Table S6: Vibrational modes of the LP phase MIL-53(Al) in the region 0–310 cm^{-1} obtained from static DFT simulations. The wavenumbers are multiplied with a scaling factor of 1.025.

Wavenumber (cm^{-1})	**Mode description**
14.6	Rotation of metal-oxide backbone + trampoline motion
38.6	Translation of metal-oxide backbone (longitudinal)
47.1	Linker rotation + rotation of octahedron
53.5/54.0/54.2	Linker rotation
59.2/60.3	Trampoline motion + scissoring of octahedron
61.9	Rotation of metal-oxide backbone
67.9	Trampoline motion
74.8	Rotation of octahedron
80.0	Rotation of octahedron + linker rotation
100.7	Rocking of metal-oxide backbone + scissoring of octahedron
105.7	Rotation of metal-oxide backbone
108.2	Linker shearing
125.7	Rocking of metal-oxide backbone + δOH
130.0	Deformation of octahedron + δOH
134.1/136.0	Linker shearing
150.8	Rocking of metal-oxide backbone + scissoring of octahedron
166.1	Scissoring of octahedron + δOH
171.5/176.1	Linker rocking
181.4	Scissoring of octahedron + seesaw motion of linker
187.3	Alternated scissoring of octahedron
188.8	Metal-oxide backbone rocking + δOH
189.9	Linker rocking
191.7	Alternated scissoring of octahedron
196.8	Deformation of octahedron through AlO_C stretching + δOH

Wavenumber (cm^{-1})	**Mode description**
212.6/213.6/220.3	Metal-oxide backbone rocking + δOH
221.7	Linker shearing + scissoring of octahedron + δOH
225.0	Scissoring of octahedron + δOH
227.4	Rocking of metal-oxide backbone + δOH
239.7	Deformation of octahedron by AlO_C stretching + δOH
252.0	Scissoring of octahedron + undulating motion of linker
253.4	Scissoring of octahedron + δOH
257.6	Scissoring of octahedron + linker rocking + δOH
260.0/262.4	Scissoring of octahedron + δOH
266.7	Linker rocking + δOH
276.0	Scissoring of octahedron + linker rocking + δOH
284.5/288.3/296.0	Metal-oxide backbone rocking + linker rocking
298.6	Scissoring of octahedron (kneecap motion)
302.5	Deformation of octahedron + linker rocking
309.5/301.2	Bending of metal-oxide backbone + scissoring of octahedron

S7 Videos of the vibrational modes

Videos of all modes discussed in this work can be found in the zip-file included in the online version of this article. The zip-file is structured as follows:

functional group vibrations (Section 4.1 in the main article)

- A1_backbone_stretch_sym.gif
- A1_backbone_stretch_as.gif
- A2_backbone_stretch_sym.gif
- A2_backbone_stretch_as.gif
- B_CH_wagging.gif
- C_CO2_bend.gif
- D_OH_bend.gif
- E_CCC_bend.gif
- F_CC_CH.gif
- G_CO2_sym.gif
- H_CC_stretch.gif
- I_CO2_as.gif

far-IR vibrations (Section 4.2 in the main article + Section S5)

- a_AlOC_front.gif
- a_AlOC_side.gif
- b_oop_front.gif
- b_oop_side.gif
- c_backbone_front.gif
- c_backbone_side.gif
- d_scissoring_OH_bend_front.gif
- d_scissoring_OH_bend_side.gif
- AlOAl_CP.gif
- AlOAl_LP.gif

collective vibrations (Section 4.4 in the main article)

- backbone_rotation.gif
- phenyl_rotation.gif
- seesaw.gif
- trampoline_LP.gif
- trampoline_CP_backbone.gif
- trampoline_CP_pore.gif

References

(1) Nevjestić, I.; Depauw, H.; Gast, P.; Tack, P.; Deduytsche, D.; Leus, K.; Van Landeghem, M.; Goovaerts, E.; Vincze, L.; Detavernier, C. et al. Sensing the framework state and guest molecules in MIL-53(Al) via the electron paramagnetic resonance spectrum of V^{IV} dopant ions. *Phys. Chem. Chem. Phys.* **2017**, *19*, 24545–24554.

(2) Liu, Y.; Her, J.-H.; Dailly, A.; Ramirez-Cuesta, A. J.; Neumann, D. A.; Brown, C. M. Reversible structural transition in MIL-53 with large temperature hysteresis. *J. Am. Chem. Soc.* **2008**, *130*, 11813–11818.

(3) Vanduyfhuys, L.; Verstraelen, T.; Vandichel, M.; Waroquier, M.; Van Speybroeck, V. Ab initio parametrized force field for the flexible metal–organic framework MIL-53(Al). *J. Chem. Theory Comput.* **2012**, *8*, 3217–3231.

(4) Debie, E.; De Gussem, E.; Dukor, R. K.; Herrebout, W.; Nafie, L. A.; Bultinck, P. A confidence level algorithm for the determination of absolute configuration using vibrational circular dichroism or Raman optical activity. *ChemPhysChem* **2011**, *12*, 1542–1549.

(5) Covington, C. L.; Polavarapu, P. L. Similarity in dissymmetry factor spectra: a quantitative measure of comparison between experimental and predicted vibrational circular dichroism. *J. Phys. Chem. A* **2013**, *117*, 3377–3386.

(6) Salazar, J.; Weber, G.; Simon, J.; Bezverkhyy, I.; Bellat, J. Characterization of adsorbed water in MIL-53(Al) by FTIR spectroscopy and ab-initio calculations. *J. Chem. Phys.* **2015**, *142*, 124702.